



**HAL**  
open science

## Numerical prediction of elastic properties for alumina green parts printed by stereolithography process

Philippe Michaud, Vincent Pateloup, Justine Tarabeux, Arnaud Alzina, Damien André, Thierry Chartier

### ► To cite this version:

Philippe Michaud, Vincent Pateloup, Justine Tarabeux, Arnaud Alzina, Damien André, et al.. Numerical prediction of elastic properties for alumina green parts printed by stereolithography process. *Journal of the European Ceramic Society*, 2021, 41 (3), pp.2002-2015. 10.1016/j.jeurceramsoc.2020.10.068 . hal-03014723

**HAL Id: hal-03014723**

**<https://unilim.hal.science/hal-03014723>**

Submitted on 3 May 2021

**HAL** is a multi-disciplinary open access archive for the deposit and dissemination of scientific research documents, whether they are published or not. The documents may come from teaching and research institutions in France or abroad, or from public or private research centers.

L'archive ouverte pluridisciplinaire **HAL**, est destinée au dépôt et à la diffusion de documents scientifiques de niveau recherche, publiés ou non, émanant des établissements d'enseignement et de recherche français ou étrangers, des laboratoires publics ou privés.

# **Numerical prediction of elastic properties for alumina green parts printed by stereolithography process**

P. Michaud<sup>a\*</sup>, V. Pateloup<sup>a</sup>, J. Tarabeux<sup>a</sup>, A. Alzina<sup>a</sup>, D. André<sup>a</sup>, T. Chartier<sup>a</sup>

<sup>a</sup> CNRS, University of Limoges, Institute of Research for Ceramics (IRCER), UMR 7315, European Ceramics Center, Limoges, France

\* Corresponding author: Philippe Michaud

\* Corresponding author E-Mail: philippe.michaud@unilim.fr

## **Keywords**

Stereolithography, Ceramic green parts, Modelling, Elastic properties

## **Abstract**

Stereolithography is a process based on the photopolymerization of a UV-reactive system consisting of ceramic particles dispersion in a curable resin. A key issue of this process is the control of the rigidity of green parts, which are strongly related to UV light exposure. This work is focused on the numerical prediction of green part stiffness according to stereolithography manufacturing parameters. A first macroscopic approach, based on the modelling of ceramic suspension polymerization, makes it possible to establish a relationship between the exposure and the Young's modulus. A second microscopic approach, using a periodic homogenization technique based on the strain energy, is applied to a 2D finite element model to evaluate the effective elastic properties. Numerical results show that macroscopic model is able to provide a Young's modulus with a good level of accuracy. The modelling results from the microscopic model demonstrate an acceptable convergence with the experimental Young's modulus.

## 1. Introduction

Stereolithography has proved to be a high-performance process for manufacturing 3D technical ceramic parts with complex architectures, a dimensional resolution up to 30 $\mu$ m, a good surface finish and mechanical properties and sintered densities similar to those obtained by conventional methods [1]. Today, this additive process is used in many fields such as biomedical, electronics, aeronautics, energy, luxury [2-8]. Stereolithography additive manufacturing is based on the selective polymerization of a curable system with a layer-by-layer construction procedure. A UV laser beam is deflected to polymerize the desired cross-sectional pattern in each layer, according to the CAD model and suitable pre-defined fabrication parameters. The curable system consists in a dispersion of ceramic particles in a sensitive monomer/oligomer with the addition of a photoinitiator. After building, the green part is cleaned (removal of the non-polymerized adherent suspension), debinded (removal of the organic phase) and sintered.

The mechanical properties of the green part will directly depend on the degree of polymerization of the curable monomer/oligomer intergranular phase, then on the fabrication parameters (i.e. laser power, laser speed, hatch spacing). For example, if the ceramic system receives too little exposure, it will not be sufficiently rigid and may break under the stress imposed by the spreading blades to deposit the thin layers. At the opposite, if the system receives too much exposure, it will be too rigid, and the part may curve during the construction (curling effect). It is also necessary to consider the shrinkage of the intergranular organic phase, which is dependent on the degree of polymerization, then on the exposure. The polymerization must therefore be homogeneous within the green part so as to avoid the creation of residual stresses, then of deformation or cracking during the post-treatments.

The objective is then to adjust the printing parameters in order to obtain a homogeneous and suitable degree of polymerization. With the aim of reaching a more homogeneous polymerization, then to decrease the risk of deformation or cracking, Chartier et al. propose, for example, low scanning speed associated to a limited power of the laser [6]. Wu et al. [9] have performed experiments on photocurable resin and have combined photopolymerization reaction kinetics with Euler–Bernoulli beam theory to study the UV post-curing induced shape distortion of thin structures prepared by DLP 3D printing and to characterize the evolution of mechanical behaviour of printed samples during the post-printing

process. The printing parameters such as printing time and height of a single-layer, post-curing UV intensity and total thickness have a significant impact on the UV-induced bending phenomenon. They concluded that the distortion of printed object depends on both the gradient of addition degree of conversion in the material during the post-curing process and the stiffness of the structure. In this respect, it appears essential to know the influence of the fabrication parameters on the distribution of the degree of polymerization inside a green part built by stereolithography, then to relate this distribution to the mechanical properties of the green part, in particular the rigidity because the green polymerized parts must be, for example, sufficient rigid to be handled [1,6]. In addition, it is essential to know the stiffness of printed green parts as input in a process simulation framework in order to evaluate residual stresses, and shrinkages or to modeling the holding during the scraping operations.

The exposure, or the density of energy, received at a specific location of the green part, is governed by the absorption and scattering phenomena of the UV light. These phenomena affect the cured volume of the part and the dimensional resolution. In addition to this geometrical consideration of the polymerized area, UV interaction with the concentrated curable suspension also influences the mechanical properties of the green part, in particular the stiffness. Indeed, the mechanical properties of the green part produced by stereolithography depend on the distribution of the monomer/oligomer degree of conversion inside the green part and therefore on the distribution of the laser exposure within the ceramic photosensitive system [10].

One pertinent approach to better understanding the physical phenomena involving during photopolymerization of a concentrated ceramic suspension, in order to optimize the stereolithography process, is numerical simulation [11]. Tarabeux et al. [12] developed a 2D numerical simulation model for predicting the curing of alumina systems, taking into account the scattering phenomenon in the stereolithography process. The simulation model makes it possible to simulate easily and with accuracy the cure width and the cure depth. This model also allows the visualization of the energy density distribution provided at each point of the part, and therefore of the corresponding degree of polymerization. Knowledge of this distribution is essential to analyze the impact of the construction layer by layer, as well as the uniformity of polymerization, and the associate shrinkage, within the part according to the manufacturing parameters. Westbeek et al. [13] proposed a 2D model, at the micro-

scale, to study photopolymerization process during additive manufacturing of green parts made of polymer resin and a maximal ceramic inclusion fraction of 40%. Their model integrates the coupled effects of light propagation through the heterogeneous matter, conversion of the photopolymer, thermal effects and evolution of mechanical properties upon solidification. The model highlights that ceramic inclusions have a marked influence for each individual physical mechanism and increase the magnitude of residual stresses in green parts. Finally, the coupled framework provides innovative insights and demonstrates that is difficult to achieve homogeneous polymerization in a ceramic-filled curable resin. Azarmi et al. [14] proposed a predictive model, to calculate overall elastic properties and thermal conductivity of alumina, that accounts for variation of the microstructure during the different manufacturing steps of laser stereolithography process. This analytical model accounts for realistic irregular shapes of the pores and is based on Maxwell homogenization theory. The values of thermal conductivity obtained by the predictive model show a very good agreement with the experimental data for sintered parts, but the values calculated for printed green parts were significantly lower than the experimentally measured ones. Concerning the Young's modulus, the values calculated with the model are in good agreement with the experimental measurements at different stages of manufacturing. This predictive model is a promising tool to estimate mechanical and thermal properties of ceramic parts manufactured by additive manufacturing. Yang et al. [15] developed two mathematical models to quantify the tensile strength and hardness of parts obtained with a pure photosensitive resin (without ceramic) used in stereolithography process. The models enable to predict the tensile strength and hardness, by considering the relationships between the degree of polymerization and mechanical properties, of both green parts and UV post-cured parts with a good accuracy. As discussed previously, the exposure values will directly influence the stiffness of green parts produced by stereolithography since the density of energy delivered will control the degree of polymerization. This degree of polymerization will evolve from the liquid monomer (Young's modulus=0) to the polymer (intrinsic Young's modulus), or more precisely a mixture of monomer/polymer with a degree of polymerization generally lower than 70-80% [10,16]. In this context, the proposed study focuses on Young's modulus prediction of alumina green parts build by stereolithography according to manufacturing parameters (laser power, laser velocity and hatch spacing). A first approach consists to establish a relation between

the exposure delivered to the curable ceramic system and the Young’s modulus of printed parts. This macroscopic approach is based on a numerical simulation model for predicting the curing of ceramic systems during the stereolithography process, developed by Tarabeux et al. [12] coupled with a mechanical characterization using image correlation technique. A second microscopic approach, considering the green part as a composite material, is developed to evaluate the elastic properties. The unit cell, considering different arrangements of ceramic grains in the resin, is analyzed using finite element method and appropriate periodic homogenization method. In this second model, perfect and rigid matrix-inclusion interfaces are considered.

**2. Method**

**2.1. Process and ceramic suspension**

Stereolithography process is based on the selective polymerization of a reactive system to build a green part, layer upon layer. The desired pattern, in each cross-sectional layer, is polymerized using the  $X/Y$  deflection of a laser beam, according to the CAD file of the part with adapted fabrication parameters (Fig. 1). The different stages of the stereolithography process are described in detail in the Tarabeux’s paper [12].

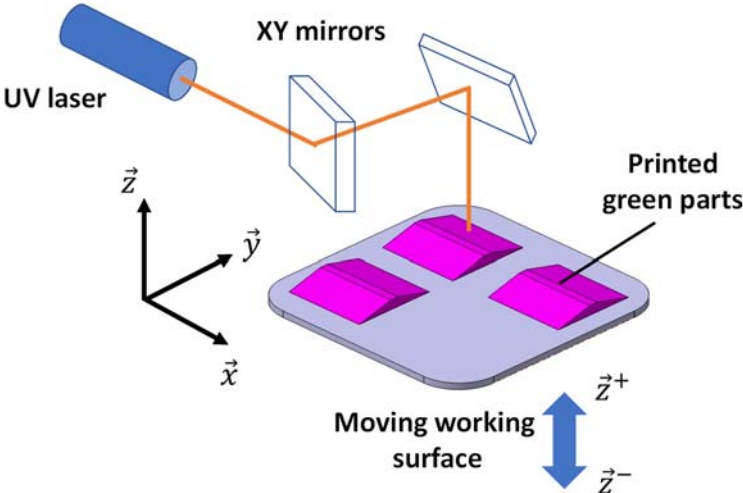


**Fig. 1.** Principle of stereolithography process

These fabrication parameters are critical, as they will control the density of energy delivered to the photopolymerizable and then the degree of polymerization. The distribution of the light exposure, or density of energy  $E$  ( $mJ/cm^2$ ), represented in Fig. 2, is defined as the laser source radiant energy per surface unit. Its expression, in the vertical plan ( $\vec{y}, \vec{z}$ ), is [12]:

$$E(y, z) = \frac{P_L}{W_0 V_L} \sqrt{\frac{2}{\pi}} \exp\left(-\frac{2y^2}{W_0^2}\right) \exp\left(-z/D_p\right) \quad (1)$$

where  $W_0$  ( $\mu m$ ) is the radius of the Gaussian laser beam,  $P_L$  ( $mW$ ) is the laser power and  $V_L$  ( $m/s$ ) the laser velocity. The parameter  $D_p$  ( $\mu m$ ) represents the penetration depth coefficient, which corresponds to the depth where the intensity of the laser beam in the reactive system, considered as a Gaussian, is reduced by  $1/e$ , compared to the intensity at the surface.

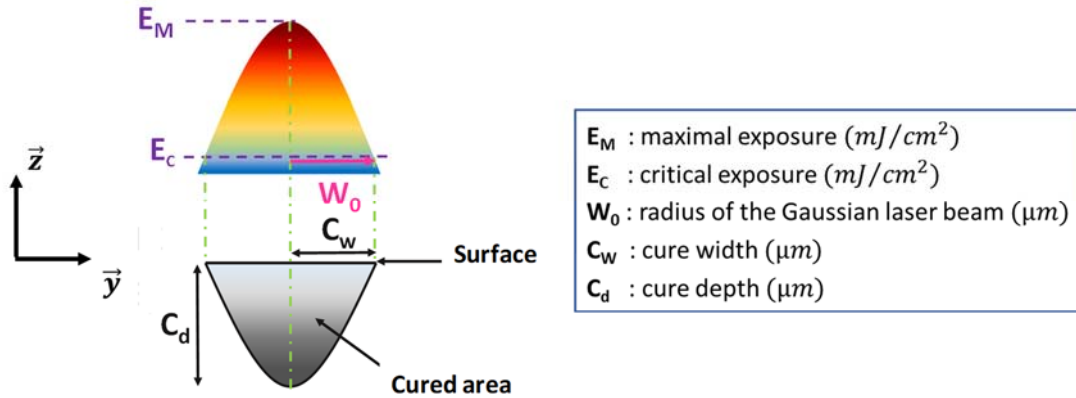


**Fig. 2.** Laser exposure distribution

$E_C$  is the critical energy, corresponding to the minimal density of energy for which polymerization occurs. The laser power  $P_L$ , the laser velocity  $V_L$  and the hatch spacing  $h$  that is the distance between two lasing lines, are three varying manufacturing parameters to be taken into account. These parameters, associated to the photosensitivity, or reactivity, of the ceramic curable suspension ( $E_C$  and  $D_p$ ), will determine the exposure and consequently the degree of polymerization and then, the stiffness of the

green parts. The influence of laser parameters, for a given alumina suspension, on the stiffness, through Young's modulus measurements has been explored.

Experimentations are carried out on green parts produced from an alumina ceramic suspension commercialized by 3DCeram-Sinto. This suspension contains 58 *vol%* of alumina with a grain size distribution:  $D_{10} = 0.5 \mu m$ ,  $D_{50} = 1.6 \mu m$ ,  $D_{90} = 4,3 \mu m$  and the used SLA system is a 3DCeram-Sinto base machine with a 355 *nm* UV laser source (Innolas Nanio AIR 355 3 W) [17].

The critical exposure  $E_C$  and the penetration depth coefficient  $D_P$  of the alumina ceramic suspension used have already been determined in previous simulation work [12]. The following paragraphs aim to predict the Young's modulus  $Y_M$  using the simulation model developed by Tarabeux et al [12].

## 2.2. Design of experiments

A design of experiments is carried out to measure the Young's modulus  $Y_{exp}$  on tensile samples with different laser powers, laser velocities and hatches spacing. The evaluation of the influence of these manufacturing parameters on the Young's modulus is conducted as precisely as possible with a Greco-Latin square design of experiments containing three factors with four laser powers, four laser velocities and three hatches spacing (Table 1). Finally, this design of experiments defines nine experiments with laser powers  $P_{L1} < P_{L2} < P_{L3} < P_{L4}$ , laser velocities  $V_{L1} < V_{L2} < V_{L3} < V_{L4}$  and hatches spacing  $h_1 < h_2 < h_3$ .

**Table 1**

Design of experiments

Experiment	E01	E02	E03	E04	E05	E06	E07	E08	E09
Laser power $P_L$ ( <i>mW</i> ) $100 \leq P_L \leq 225$	$P_{L2}$	$P_{L2}$	$P_{L1}$	$P_{L3}$	$P_{L3}$	$P_{L3}$	$P_{L4}$	$P_{L4}$	$P_{L4}$
Laser velocity $V_L$ ( <i>m/s</i> ) $2500 \leq V_L \leq 5500$	$V_{L1}$	$V_{L2}$	$V_{L4}$	$V_{L1}$	$V_{L2}$	$V_{L3}$	$V_{L1}$	$V_{L2}$	$V_{L3}$
Hatch spacing $h$ ( $\mu m$ ) $20 \leq h \leq 40$	$h_1$	$h_2$	$h_1$	$h_2$	$h_3$	$h_1$	$h_3$	$h_1$	$h_2$

### 2.3. Microscopic observations

In order to investigate the microstructure of green parts after printing, SEM micrographs have been observed for the nine cases of design experiment. The green parts are metallized with platinum on a slice perpendicular to the building direction. Only the two SEM micrographs, at different magnifications, corresponding to E03 experiment are presented in Fig.3 because microstructures of the nine SEM micrographs are very similar. A very low number of pores is observed in Fig. 3 (a). It is recognized that during the stereolithography process, the resin fills all the spaces between the ceramic particles and that the green part consists in bi-component system (i.e. ceramic particles, polymerized resin) without remaining porosity. The few visible pores observed in the green parts may be due to the bubbles initially present in the ceramic suspension. In Fig. 3 (b), the dark areas correspond to the polymer resin and the wider areas, surrounded by a white line, are mainly due to defects in the arrangement of inclusions. The observed general shape of inclusions is close to polyhedral shape. The SEM micrographs of the nine cases of design experiment showed that the grain size is between 0.2 and 5  $\mu\text{m}$ . No microcracks within the polymerized resin and at the inclusions-resin interface appear. The Fig. 3 (a) also shows a good adhesion between layers with a thickness equal to 50  $\mu\text{m}$  as no interfaces between layers are visible.

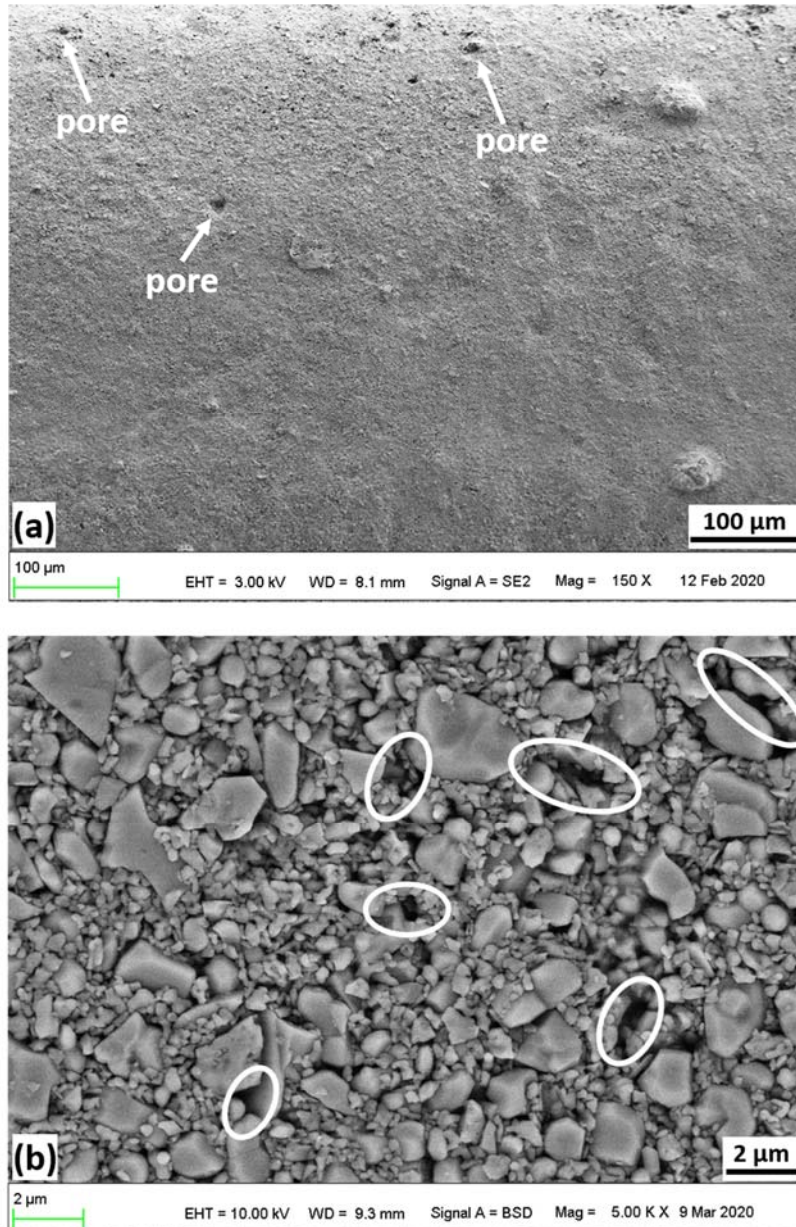


**Fig. 3.** SEM micrographs of green alumina parts corresponding to E03 experiment

(a) : low magnification and (b) : high magnification

#### **2.4. Tensile test and image correlation technique**

Digital image correlation (DIC), a non-contact optical method, is an effective tool to measure quantitative deformation of a planar object surface. This method provides, in a specific zone of interest, full-field displacements with sub-pixel accuracy and full-field strains by comparing the digital images of a test object surface acquired before and after deformation [18]. This technique, coupled with tensile tests, makes it possible to identify the law behaviour and mechanical properties of materials [19].

Concerning the DIC technique, a camera placed in front of a speckled sample's surface, takes digital images regularly during testing and a correlation algorithm, developed at the IRCER Institute, compares digital images of the reference state and of the deformed one. The speckle pattern, which deforms together with the specimen surface as a carrier of deformation information, is required to enable the algorithm to directly measure the displacement fields between images and to evaluate the deformation  $\epsilon$  during testing [18]. A random black speckle pattern is then printed on the white surface ( $13 \times 2 \text{ mm}^2$ ) of the alumina green samples. Before testing, every sample is properly placed on the tensile testing fixture and is tightened with a dynamometric key.

The tensile test was conducted using a micro-device developed by DEBEN UK Ltd with a maximum  $2 \text{ kN}$  load capability. The loading rate of the upper crosshead was set as  $0.2 \text{ mm/min}$ . For each experiment of the design of experiments, four samples have been tested to insure the reproducibility.

The tensile micro-device, the camera used ( $2500 \text{ pixels} \times 1920 \text{ pixels}$ ) and the printed samples are presented in Fig. 4.

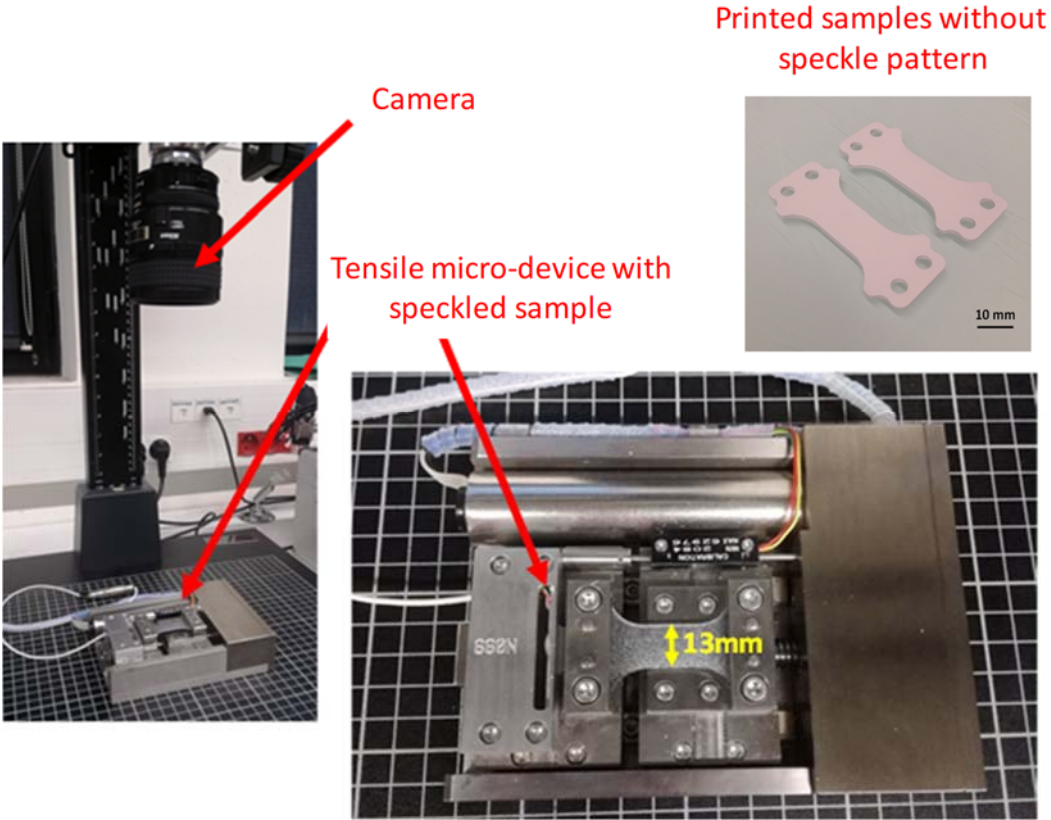


Fig. 4. Tensile micro-device and printed green parts

Once the data has been recorded and analyzed, the Young's moduli have been calculated in the linear part of the stress-strain curves (Fig. 5).

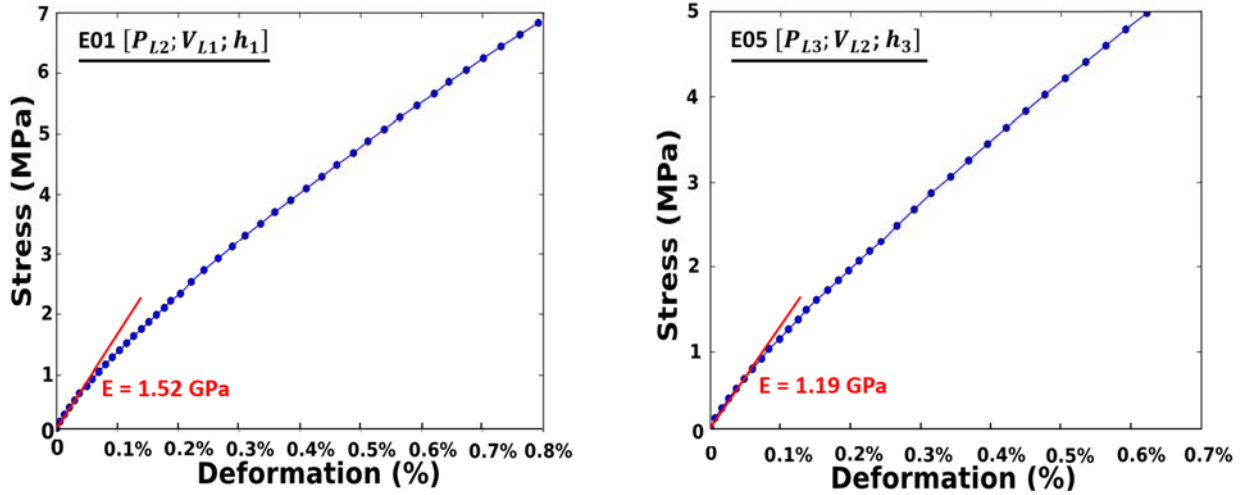


Fig. 5. Stress-strain curves and Young's modulus

## 2.5. Numerical modelling

### 2.5.1. Exposure simulation

The objective is to correlate the value of the Young's modulus  $Y_M$  to the laser exposure  $E(y, z)$ , which depends on process parameters. The scattering phenomenon, due to the presence of ceramic particles in the photopolymerizable system, will also depend on the density of energy delivered. Scattering is considered by introducing a scattering factor  $F_{scatt}$ , which corresponds to an expansion of the laser beam radius ( $W_{0corr}$ ) [12].

$$F_{scatt} = \frac{W_{0corr}}{W_0} \quad (2)$$

The expression for the exposure  $E(y, z)$  becomes:

$$E(y, z) = \frac{P_L}{W_0 F_{scatt} V_L} \sqrt{\frac{2}{\pi}} \exp\left(-\frac{2y^2}{(W_0 F_{scatt})^2}\right) \exp\left(-z/D_p\right) \quad (3)$$

In previous work [12], a numerical model has been developed to predict the cure depth  $C_d$  and the cure width  $C_w$  from the simulation of the laser exposure. This numerical model is based on summing up all the exposures received at each pixel of the reactive system for all passages of the moving laser beam. The overall exposure received is thereby known for every pixel and the polymerization condition ( $E(y, z) > E_C$ ) is applied to determine the cured areas.

By observing the scattering phenomenon during several previous experiments and analyzing its evolution, a scattering law that follows a logarithmic law and that is exposure-related (Eq. 4) has been proposed and validated during the simulation model development.

$$F_{scatt} = a \log(E_{M1l}) + b \quad \text{with } a > 0 \text{ and } b < 0 \quad (4)$$

where  $E_{M1l}$  represents the overall maximum exposure delivered on one-layer for all the lasing lines.

After the identification of the specific parameters of the alumina curable ceramic suspension ( $E_C$  and  $D_p$ ) and the assessment of the scattering factor  $F_{scatt}$  with  $a$  and  $b$ , the simulation model has been validated for several laser parameters to accurately evaluate both the cure depth and the cure width [12].

### 2.5.2. Young's modulus prediction of green parts with macroscopic model

The numerical model, developed to simulate the exposure distribution, is a relevant tool for predicting the stiffness of green parts manufactured by stereolithography. Indeed, Jacob [10] proposed a relation (Eq. 5) between the Young's modulus and the maximum exposure for a pure photopolymerizable resin.

$$Y_M = Y_{M\_max} \left( 1 - \exp \left( -\beta \left( \frac{E_M}{E_C} - 1 \right) \right) \right) \quad \text{with } \beta = \frac{K_p \cdot E_C}{Y_{M\_max}} \quad (5)$$

The maximal Young's modulus  $Y_{M\_max}$  is the maximal value deduced from experimental results. The parameter  $\beta$  is dimensionless and depends on the critical exposure  $E_C$ , the maximal Young's modulus  $Y_{M\_max}$  and a photomodulus coefficient  $K_p$ . This latter corresponds to the slope at the beginning of the

curve  $Y_M = f(E)$  (just above zero), where  $Y_M(E)$  is zero (for  $E < E_C$ , the non-polymerized resin remains liquid).

One of issues of this work is to define a new model adapted to the ceramic systems in order to establish a relation between the Young's modulus and the exposure received by the green parts.

### **2.5.3. Elastic properties prediction of green parts with microscopic model**

Composites are generally characterized by strong heterogeneities at the microscopic scale. The classical computational modelling used at the macroscopic scale cannot be applied to this kind of materials because they are not enabled to cover the microstructural mechanisms which are essential to the understanding of the macroscopic behaviour. In the context of finite element simulation this requires, for example, extremely fine meshes to represent the corresponding geometry and kinematic. To overcome this problem, some analytical and numerical homogenization techniques have been developed. The goal of the homogenization method is to replace a real heterogeneous material by an equivalent fictitious homogeneous material. Concerning the case of particulate micro-composites, an interesting category of analytical models is the category of bounds models providing the extrema behaviour of the composite. The simplest ones consider parallel and serial associations of the two phases. Considering the elasticity, these limits are the Voigt and Reuss bounds [20], corresponding to rules of mixtures for stiffness and compliance components, respectively. For instance, the model proposed by Hashin and Shtrikman [21-23] is dedicated to isotropic and transverse-isotropic materials composed of a matrix and inclusions with perfect matrix-inclusion interfaces. These analytical models, called uniform field models, present some restrictions because they do not account for local variations in the strain and stress fields [24].

To overcome these restrictions, numerical homogenization techniques which not use simplifying assumptions are based first and foremost on the choice of "Representative Elementary Volume (RVE)" or "Unit Cell" which is related to the domain size of a microstructure providing a good statistical representation of the material properties. The size of this RVE represents an essential element to determine the effective properties and depends on the nature of the constituents of the material studied. Some definitions have been proposed for the concept of the RVE [25-31]. All the definitions agree that

this RVE must contain sufficient information on the microstructure while being very small compared to the dimensions of the structure at a macroscopic scale. Kanit et al. [29] reported that the volume of RVE cannot be taken as small as desired, as there is generally some influence of the RVE volume due to the type of boundary conditions chosen in the property estimation of the properties. Average apparent properties calculated on finite size domains do not match effective properties if the size of the domain is too small. So, a numerical procedure was proposed to determine the critical size of RVE for random composites [29]. This procedure includes the following first steps which are necessary to evaluate the critical size RVE, i) the generation of different microstructures for 4–5 different volume sizes, ii) the loading of each microstructure with boundary conditions, iii) the calculation of the mean value and variance of apparent property for the considered volume sizes and iv) the checking that the number of generated microstructures is sufficient for each volume. The critical size of the RVE is dependent on the difference of the mechanical properties between the phases constituting the material. Pelissou et al. [32] proposed a new method to determine the critical size of RVE for a quasi-brittle random metal matrix composite, for linear and non-linear properties, by applying periodic boundary conditions. This method is based on the classical geostatistical framework previously used by Kanit et al. [29] and on a new stopping criterion based on the estimation error but integrating the uncertainty due to the limited size of samples. Some works have been focused on the elastic behaviour of materials reinforced with hard spherical particles, on polymer matrix-reinforced composites and on porous materials [33-36]. The authors showed, for linear elastic materials, that particle size has a slight effect on the evaluation of effective properties and that the most important is to respect the volume fraction of inclusions. The effect of the spatial distribution of inclusions in a matrix with no contact between inclusions has been analyzed [33, 37, 38]. The results showed that the distribution of spherical inclusions does not influence significantly the macroscopic behaviour.

Numerical homogenization techniques depend, in addition to the RVE size, on the choice of boundary conditions to be applied. Three classical boundary conditions, namely the Kinematic uniform boundary conditions KUBC, the Static uniform boundary conditions SUBC and the periodic boundary conditions are generally used. In the case of linear elasticity, the KUBC boundary conditions overestimate the effective properties, while the SUBC boundary conditions underestimate them. The estimation of

effective properties using the periodic boundary conditions then appears more accurate than using SUBC and KUBC conditions [29]. Other numerical studies [39-41] also confirm that periodic boundary conditions provide a better estimation of effective properties even if the microstructure is not perfectly periodic.

A green part manufactured by stereolithography can be considered as random distribution of ceramic particles in a polymeric phase. It is then possible to determine the effective elastic properties of this particulate composite by applying the homogenization technique coupled with a finite element model. In order to evaluate the effective elastic properties of alumina green parts, the minimum size of RVE, by applying periodic boundary conditions, is firstly determined by studying the convergence of components of stiffness matrix in function of the size of RVE. Then, the material symmetry of the homogenized equivalent medium is analyzed to determine the elastic properties.

#### **2.5.3.1. Generation of microstructures: random distribution and classical arrangements**

The shape of the particles can affect the overall elastic properties of particulate composites especially when large particles with a high aspect ratio are oriented. In this case, the mechanical behaviour of these material composites is anisotropic. The shape effect might become much more significant when considering non-linearities (debonding of the particles, matrix plasticity or failure) due to different stress concentrations around these particles. In the case of 2D modelling, Gentieu et al. showed that particulate composites constituted of a soft matrix (3 GPa) and stiff polygonal or circular shaped inclusions (450 GPa) give, for volume fractions lower than 60%, close elastic properties [24]. As the shape of the inclusions has a small effect on the effective elastic properties, ceramic inclusions are so considered spherical despite a polyhedral shape observed in Fig. 3 (b). The ceramic inclusions are so ideally modeled by disks (2D) in order to simplify the generation of inclusions and are completely embedded in the RVE or elementary cell representing the cured resin. The random distribution of ceramic inclusions in the unit cell was obtained thanks to an internal code, developed with Python language and Salome-Meca software [42], by integrating the random sequential adsorption algorithm called “RSA” [43-45]. The disks are randomly placed in the defining cell rejecting those that overlap with previously placed ones, and so on until the desired volume fraction of inclusions in the matrix is achieved. No

contact is allowed between the inclusions themselves and between the inclusions and the edges of the RVE. The RVE was generated with a volume fraction of 58% ( $\pm 0.5\%$ ) and for reasons of simplicity, 3 inclusion diameter sizes are chosen, i.e. equal to  $1\ \mu\text{m}$ ,  $2\ \mu\text{m}$  and  $5\ \mu\text{m}$ . The real alumina grain size distribution is not totally respected, but we have seen that the particle size does not influence the effective properties evaluation [33-35]. In order to simplify the numerical model, a perfect interface between the polymeric matrix and ceramic inclusions is supposed, which may be a strong assumption. Before calculating the effective elastic properties, the first step is to determine the minimum size of the RVE able to represent finely and correctly the macroscopic response of the composite material. The edges of the RVE vary from  $20\ \mu\text{m}$  to  $100\ \mu\text{m}$  (Fig. 6). Once the minimum size of the RVE is defined, the effective Young's modulus obtained with a random distribution and classical arrangements is compared with experimental results. The square and hexagonal arrangements, represented in Fig. 7, are respectively assimilated to cubic and face-centred cubic arrangements which exhibit a cubic symmetry behaviour.

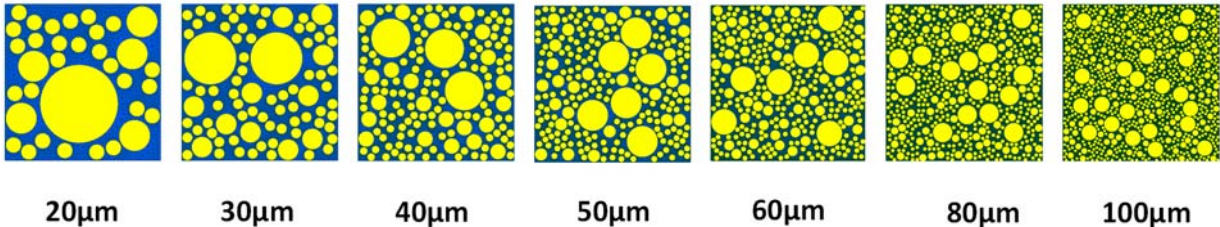


**Fig. 6.** Different RVE sizes of random distribution

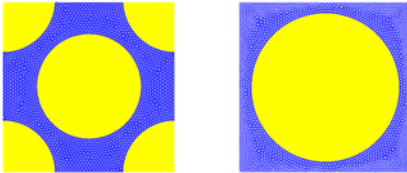


**Fig. 7.** Modelled RVE corresponding to hexagonal (left) and square (right) arrangements

The RVE is meshed with plane linear triangular elements with an average element size varying from  $\text{RVE\_edge}/40$  to  $\text{RVE\_edge}/200$  respectively for RVE size varying from  $20\ \mu\text{m}$  to  $100\ \mu\text{m}$ . A special

attention, for random microstructures, has been paid to the fact that no element of meshes was distorted due to the small size of inclusions.

### 2.5.3.2. Homogenization method

#### 2.5.3.2.1. RVE Equilibrium state

Considering the representative volume element of microstructures (Fig. 6 and Fig. 7), the equilibrium equations, in absence of body forces, is defined by:

$$\sigma_{ij} = \frac{\partial w}{\partial \varepsilon_{ij}} \quad (6)$$

where  $\sigma_{ij}$ ,  $\varepsilon_{ij}$  and  $w$  are the local stress tensor, the local strain tensor and local strain energy density, respectively.

#### 2.5.3.2.2. Average theory

Averaging relations at the microscopic scale makes it possible to establish relation between the stresses and the strains at this microscopic scale and their equivalents at the macroscopic scale using the following expressions [46]:

$$\bar{\sigma}_{ij} = \frac{1}{S} \int_S \sigma_{ij} dS \quad (7)$$

$$\bar{\varepsilon}_{ij} = \frac{1}{S} \int_S \varepsilon_{ij} dS \quad (8)$$

$\sigma_{ij}$ ,  $\varepsilon_{ij}$  are the actual local stress and strain tensor components in the RVE, respectively.

$\bar{\sigma}_{ij}$  et  $\bar{\varepsilon}_{ij}$  are the macro-stress and macro-strain over the surface  $S$  of the RVE, respectively.

### 2.5.3.2.3. Periodic boundary conditions applied to the RVE

Since the periodic boundary conditions are applied to the RVE, the displacement field for a two-dimensional periodic structure can be decomposed as follow:

$$u_i(x_1, x_2) = \bar{\varepsilon}_{ij} \cdot x_j + u_i^*(x_1, x_2) \quad (9)$$

The 1<sup>st</sup> and 2<sup>nd</sup> terms on the right of the Eq. 9 represent, respectively, a linear displacement field and a periodic function from one RVE to another. The latter is the periodic fluctuation of the linear displacement field due to the heterogeneities. From this equation, the periodic fluctuation of the displacement field can be deduced:

$$u_i^*(x_1, x_2) = u_i(x_1, x_2) - \bar{\varepsilon}_{ij} \cdot x_j \quad (10)$$

To apply this type of condition, two neighboring cells in their deformed state must always coincide along their common edge without overlapping. The continuity of the stress vector  $\sigma \cdot \vec{n}$  ( $\vec{n}$  is the normal vector at the considered edge) and the compatibility of the strain fields (no separation and no overlap of neighboring RVE are allowed) must be therefore ensured. The corresponding periodic boundary conditions are presented in a square RVE in Fig. 8.

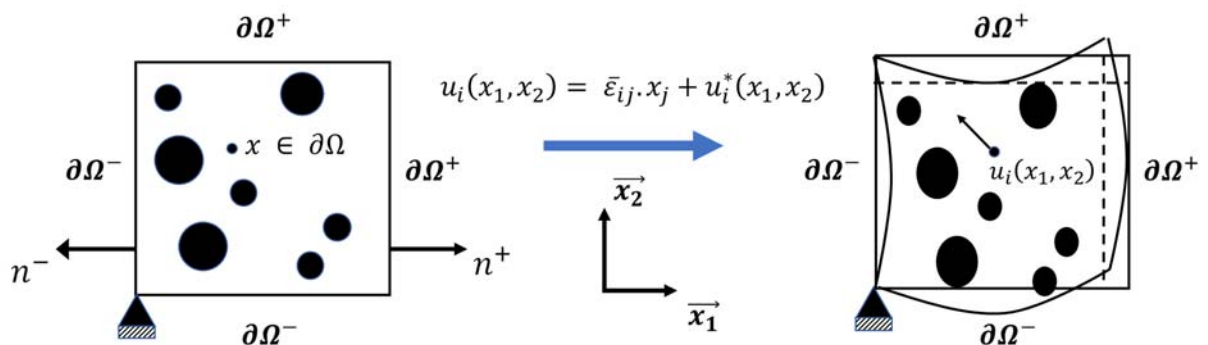


**Fig. 8.** Periodic boundary conditions on RVE

$\partial\Omega$ ,  $\partial\Omega^-$  and  $\partial\Omega^+$  are the domain and opposite edges of the RVE, respectively.

The boundaries of the RVE can be divided into pairs of opposite edges  $\partial\Omega^-$  and  $\partial\Omega^+$ . According to Eq. 10, the displacements on the boundaries of the RVE are then defined by:

$$u_i^*(x_1, x_2)^- = u_i(x_1, x_2)^- - \bar{\varepsilon}_{ij} \cdot x_j^- \quad (11)$$

and

$$u_i^*(x_1, x_2)^+ = u_i(x_1, x_2)^+ - \bar{\varepsilon}_{ij} \cdot x_j^+ \quad (12)$$

the condition  $u_i^*(x_1, x_2)^- = u_i^*(x_1, x_2)^+$  must be satisfied on the domain  $\partial\Omega$  [47], we thus obtain:

$$u_i(x_1, x_2)^+ - u_i(x_1, x_2)^- = \bar{\varepsilon}_{ij} \cdot (x_j^+ - x_j^-) \quad (13)$$

However, this last boundary condition may not be complete or not guarantee the conditions of continuity of traction, which can be written:

$$\sigma_n^+ - \sigma_n^- = 0 \quad \text{and} \quad \sigma_t^+ - \sigma_t^- = 0 \quad (14)$$

where  $\sigma_n$  and  $\sigma_t$  are the normal and tangential stresses applied on the parallel edges of the RVE, respectively.

To apply these different boundary conditions, the distribution of the nodes on two opposite edges of the RVE must be identical. This ensures a periodic mesh and the displacements of the corresponding nodes of each opposite side can thus be coupled.

#### 2.5.3.2.4. Estimation of the effective stiffness tensor

The effective stiffness tensor of the homogeneous equivalent material is determined from an energy analysis. The fundamental hypothesis of homogenization is the equivalence of the strain energies at the microscopic and macroscopic scales.

$$\frac{1}{2} \int_S \sigma_{ij} \varepsilon_{ij} dS = \frac{1}{2} \bar{\sigma}_{ij} \bar{\varepsilon}_{ij} S \quad (15)$$

This requirement is expressed by Hill's condition [48], which states that the average quantities of stresses and strains guarantee the equivalence of strain energy between the homogeneous equivalent material and the original heterogeneous material.

For linear elastic anisotropic materials, the homogenized stiffness matrix  $C_{ijkl}$  of the considered RVE is defined by the linear relation of the macroscopic stress and strain tensors:

$$\bar{\sigma}_{ij} = C_{ijkl} \bar{\varepsilon}_{kl} \quad (16)$$

In the case of plane strains, Eq. 16 can be written, in Voigt notation:

$$\begin{pmatrix} \bar{\sigma}_1 \\ \bar{\sigma}_2 \\ \bar{\sigma}_6 \end{pmatrix} = \begin{pmatrix} C_{11} & C_{12} & C_{16} \\ C_{12} & C_{22} & C_{26} \\ C_{16} & C_{26} & C_{66} \end{pmatrix} \begin{pmatrix} \bar{\varepsilon}_1 \\ \bar{\varepsilon}_2 \\ \bar{\varepsilon}_6 \end{pmatrix} \quad (17)$$

Where  $\bar{\sigma}$  and  $\bar{\varepsilon}$  are the stresses and strains tensors, respectively.  $C_{ij}$  are the components, in the contracted form, of stiffness tensor.

The total strain energy stored in the homogenized RVE is defined by:

$$U = \frac{1}{2} \bar{\sigma}_{ij} \bar{\varepsilon}_{ij} S \quad (18)$$

or

$$U = \frac{S}{2} C_{ijkl} \bar{\varepsilon}_{ij} \bar{\varepsilon}_{kl} \quad (19)$$

In practice and for linear elastic materials, the strain energy is obtained by finite element calculations for different states of imposed strain, allowing to activate only certain components of the stiffness tensor. The stiffness matrix at the macroscopic scale can be therefore identified, with its 9 constants in the 2D case. For example,

$$\bar{\varepsilon} = \begin{pmatrix} 1 & 0 & 0 \\ 0 & 0 & 0 \\ 0 & 0 & 0 \end{pmatrix} \quad (20)$$

the elastic strain energy calculated on the RVE is equal to:

$$U = \frac{1}{2} S C_{11} \quad (21)$$

from which  $C_{11}$  is calculated.

The other components of the stiffness matrix at the macroscopic scale are calculated in a similar way by imposing the state of corresponding strain.

### 3. Results

#### 3.1. Experimental results

The Fig. 9 represents the average values and the standard deviations of the Young's modulus experimentally measured for each experiment presented in Table 1. The measured values of the Young's modulus are between 0,97 GPa and 1,58 GPa, which means that the green parts printed by the stereolithography process are not very rigid. The prediction of the Young's modulus is therefore essential to ensure the mechanical strength of the part during printing and therefore the feasibility of manufacturing, but also the handling of green parts during the cleaning step. Then a first conclusion is that values of Young's modulus vary by a factor of 1.5, which depends on the manufacturing parameters.

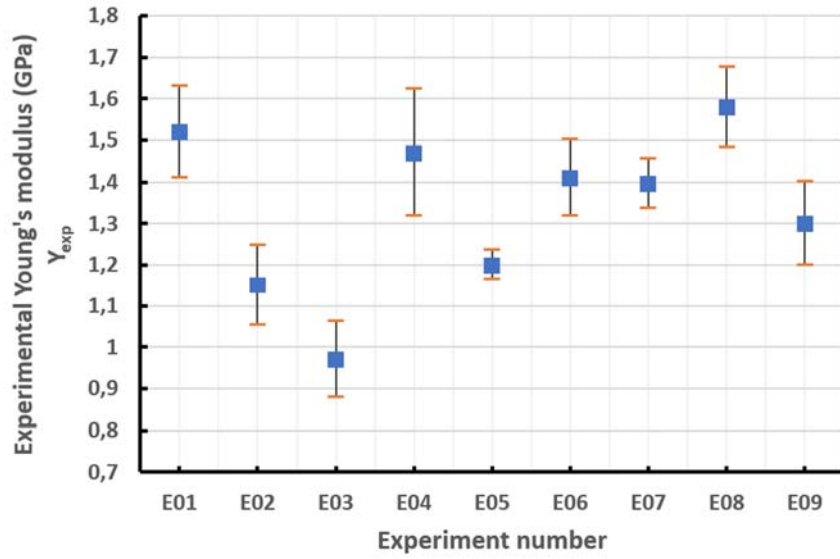


**Fig. 9.** Experimental Young's modulus of printed green parts with standard deviations

### 3.2. Macroscopic modelling

#### 3.2.1. Young's modulus prediction of green parts

One objective of this study is to offer a macroscopic model that establishes a relation between the exposure received during the manufacturing and the Young's modulus of green parts. The evolution of experimentally measured Young's modulus compared to overall maximum exposure computed with the numerical model developed by Tarabeux et al. [12] is represented in Fig. 10. A quasi-linear evolution on a logarithmic scale of the experimental Young's modulus as a function of overall maximum exposure for 10 layers  $E_{M10l}$ , assimilated to the maximal exposure  $E_M$ , can be observed. A logarithmic law is therefore appropriate to describe the evolution of Young's modulus of ceramic green parts as a function of the exposure. The curve cut the horizontal axis for  $20 \text{ mJ/cm}^2$ , corresponding to the Young's modulus equal to zero, which is very close to the critical exposure value of alumina system equal to  $17 \text{ mJ/cm}^2$  [12]. When the value of the exposure is lower than the critical exposure  $E_C$ , the photosensitive system is not cured (liquid monomer/oligomer) and therefore does not exhibit mechanical resistance. The relation between the Young's modulus  $Y_M$  and the overall maximum exposure  $E_M$  can be written:

$$Y_M = F_{stiff} \ln(E_M/E_C) \quad (22)$$

$F_{stiff}$  represents the rigidity factor and corresponds to the slope of the  $Y_M = f(\ln E_M)$  curve. This rigidity factor can be considered as a “specific mechanical property” of the green part and is equal to 0,476 GPa in our case. This relation is different than this one proposed by Jacob (Eq. 5). It can be explained by the presence of ceramic particles in the polymeric phase.

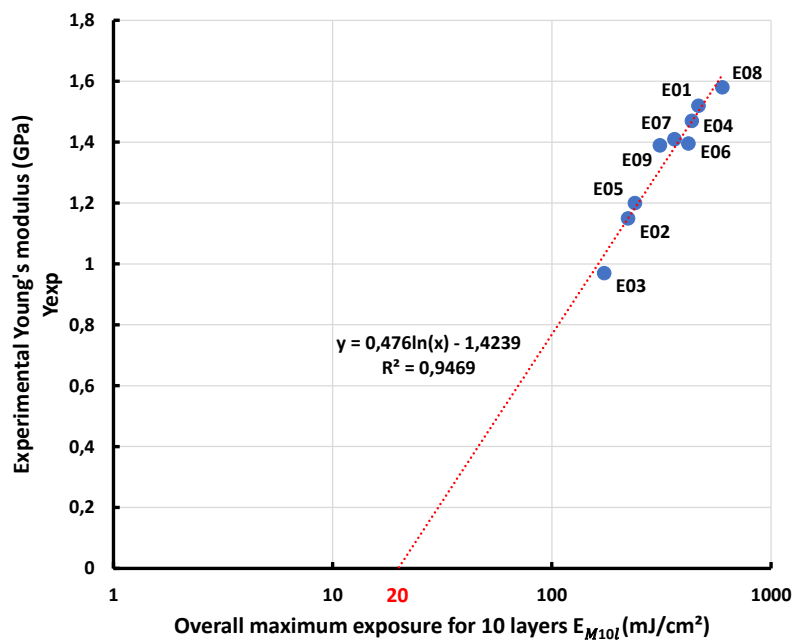


**Fig. 10.** Experimental Young’s modulus of printed green parts according to overall maximum exposure for 10 layers  $E_{M10l}$

A very good agreement is observed between the experimental Young’s modulus and calculated values using the macroscopic model with a maximal relative error equal to 6% corresponding to E07 experiment (Fig. 11).

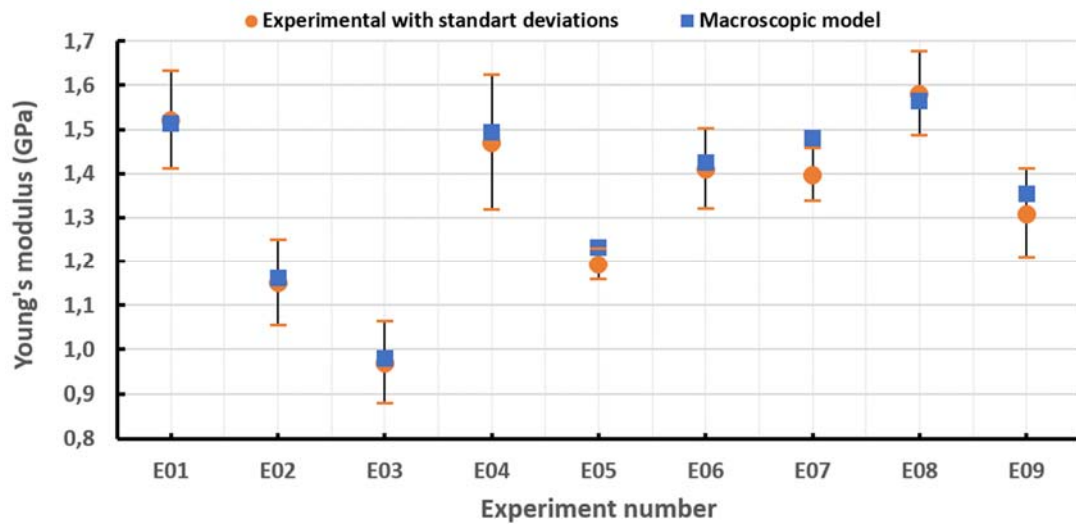


**Fig. 11.** Comparison between experimental and simulated Young's moduli according to manufacturing parameters

### 3.2.2. Young's modulus prediction of resin

Another objective of this study is to propose a microscopic model that determine the elastic properties of ceramic green parts manufactured by stereolithography by applying the homogenization technique. In this case, the knowledge of mechanical properties of the resin is necessary for the microscopic model. Mechanical properties of the resin will depend on the degree of conversion and vary therefore according to manufacturing parameters. The tensile test coupled to the DIC technique is also used for the pure resin, as for the green parts, to measure the Young's modulus of the matrix and to identify the coefficient  $K_p$  (Eq. 5). Three new experiments (ER01, ER02, ER03), corresponding to manufacturing parameters for which the resin parts are rigid, are conducted. Four samples have been tested for each experiment. The Fig. 12 represents the evolution of Young's modulus, for the three news experiments, with standard deviations according to overall maximum exposure for ten layers  $E_{M10l}$ . The "photomodulus" coefficient  $K_p$  of the resin, equal to  $6 \cdot 10^5 m^{-1}$ , corresponds to the initial increase rate of the Young's modulus. The photomodulus coefficients of resins reported by Jacob's [10] are between  $1,6 \cdot 10^5 m^{-1}$  and  $8,7 \cdot 10^5 m^{-1}$ . A high value of  $K_p$  accounts for, during the polymerization, strong and numerous bonds making the polymer structure more rigid. The value of exposure, for a null Young's modulus, is

30  $mJ/cm^2$ . This value agrees with the value of the critical exposure of the unloaded system reported, i.e 38,3  $mJ/cm^2$  [49].

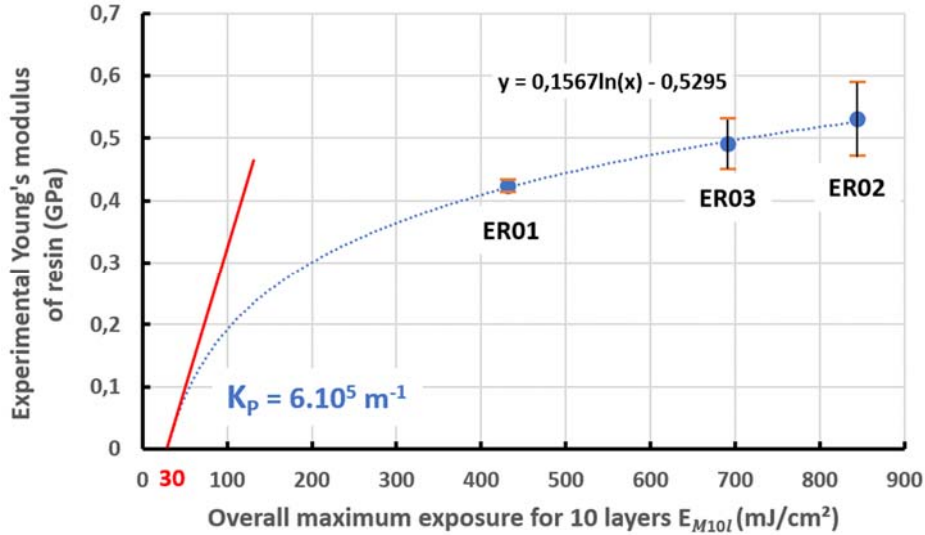


**Fig. 12.** Evolution of Young's modulus pure resin according to overall maximum exposure for 10 layers  $E_{M10l}$  and identification of the coefficient  $K_p$

The determination of Young's modulus values of the pure resin, according to manufacturing parameters of ceramic green parts (Table 1), was performed by using the matching curve of the Young's modulus function of the overall maximum exposure for 10 layers  $E_{M10l}$  plotted in Fig. 12. This method, for the E01, E02, E03, E06 and E08 manufacturing conditions, is presented in Fig. 13 (the plotting of the other experiments is not presented to have a readable figure). The overall maximum exposure for 10 layers  $E_{M10l}$  according to manufacturing parameters and the corresponding Young's modulus values of the pure resin are listed in the Table 2. These results highlight the effect of the exposure on the Young's modulus. Over the measuring range, the higher the exposure, the stiffer the ceramic green parts.

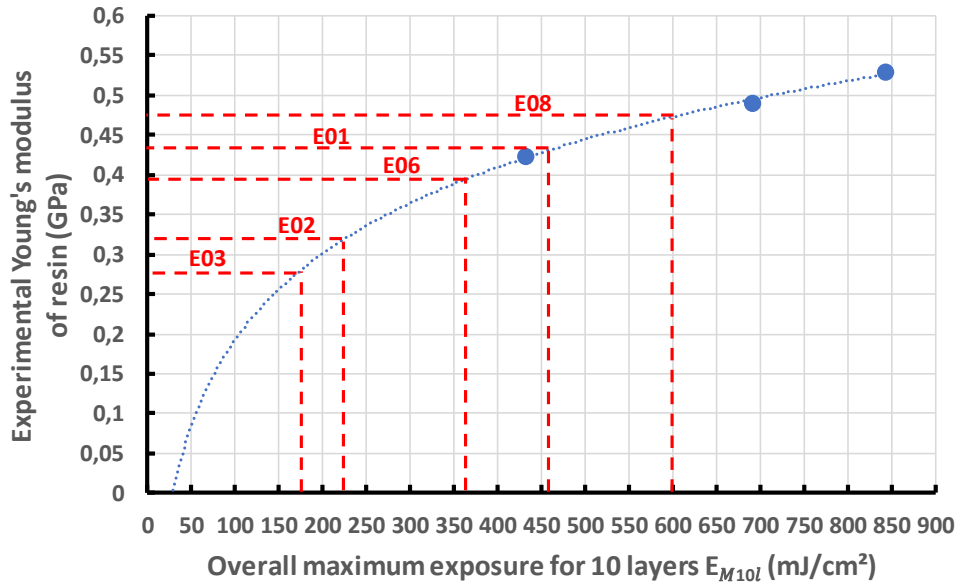


**Fig. 13.** Evolution of the Young's modulus of pure resin according to overall maximum exposure for 10 layers  $E_{M10l}$

**Table 2**

Young's modulus of the pure resin according to manufacturing parameters of green ceramic parts

Experiment	E01	E02	E03	E04	E05	E06	E07	E08	E09
Laser power $P_L$ (mW)	$P_{L2}$	$P_{L2}$	$P_{L1}$	$P_{L3}$	$P_{L3}$	$P_{L3}$	$P_{L4}$	$P_{L4}$	$P_{L4}$
Laser velocity $V_L$ (m/s)	$V_{L1}$	$V_{L2}$	$V_{L4}$	$V_{L1}$	$V_{L2}$	$V_{L3}$	$V_{L1}$	$V_{L2}$	$V_{L3}$
Hatch spacing $h$ ( $\mu\text{m}$ )	$h_1$	$h_2$	$h_1$	$h_2$	$h_3$	$h_1$	$h_3$	$h_1$	$h_2$
Overall maximum exposure for 10 layers $E_{M10l}$ (mj/cm <sup>2</sup> )	466	222	173	435	239	362	419	599	310
Young's modulus of pure resin (GPa)	0,43	0,32	0,28	0,42	0,325	0,395	0,415	0,47	0,37

### 3.3. Microscopic modelling

The generated RVE and the computing of effective elastic properties of the green parts printed by stereolithography have been performed in the plane  $(\vec{x}_1, \vec{x}_2)$ , perpendicular to printing direction (Fig. 14). The useful mechanical properties of the resin matrix and of the alumina inclusions, are listed in Table 3. For the resin matrix, the Young's modulus and the Poisson's ratio are from our experimental

results and from the literature [13,50] respectively. Concerning alumina inclusion, the mechanical properties are from 3DCeram-Sinto [17].

**Table 3**

Useful mechanical properties of each phase composing printed green parts

Phase	Mechanical symmetry	Young's modulus E	Poisson's ratio $\nu$
Polymer resin matrix	Isotropic	0,4 GPa	0,40
Alumina inclusion	Isotropic	350 GPa	0,25

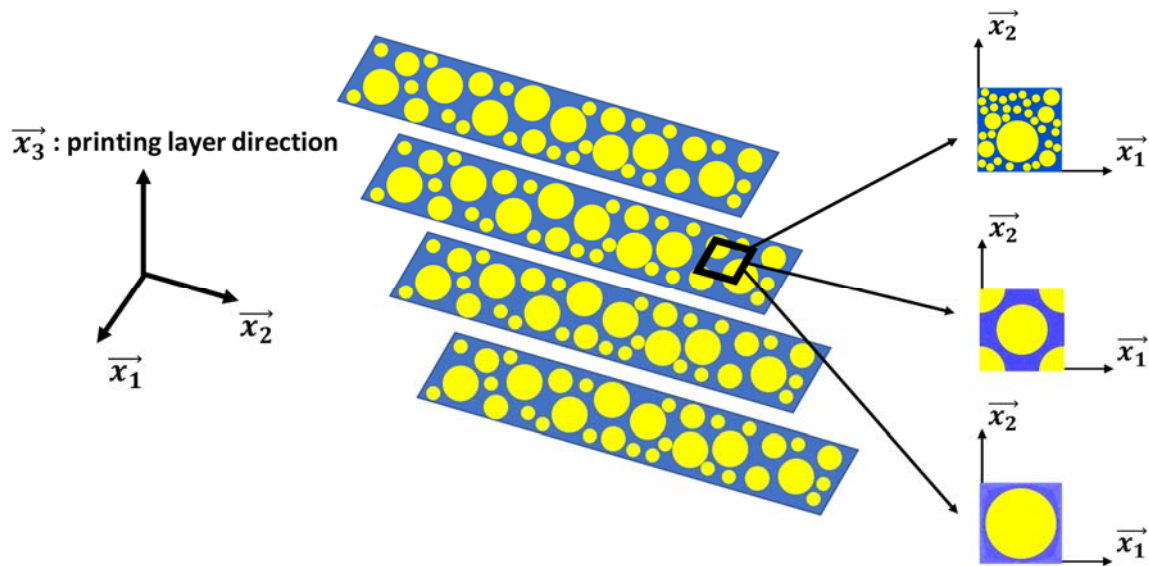


**Fig. 14.** Printing layer direction and 2D generated RVE

### 3.3.1. Determination of the minimum size of RVE and its mechanical symmetry

The evolutions, according to RVE size, of the following ratios of the stiffness matrix components  $C_{22}/C_{11}$ ,  $2 C_{26}/(C_{11} - C_{12})$ ,  $C_{26}/C_{11}$  and  $C_{16}/C_{11}$  are analyzed in order to determine the minimum size of RVE and to evaluate the material symmetries of the homogenized equivalent medium. For an isotropic elastic material, the first two ratios must be equal to one while the last two must be null [36]. For the seven different RVE sizes, ten random microstructures are generated. The

average, for each of the ten microstructures, and corresponding standard deviations are presented in Fig. 15 and Fig. 16.

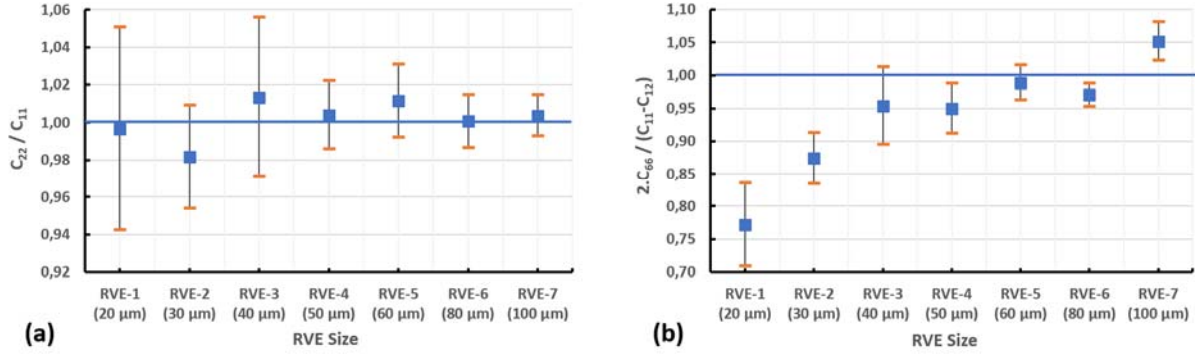


**Fig. 15.** Variation of the ratios  $C_{22}/C_{11}$  (a) and  $2.C_{66}/(C_{11} - C_{12})$  (b) with standard deviations according to the RVE size

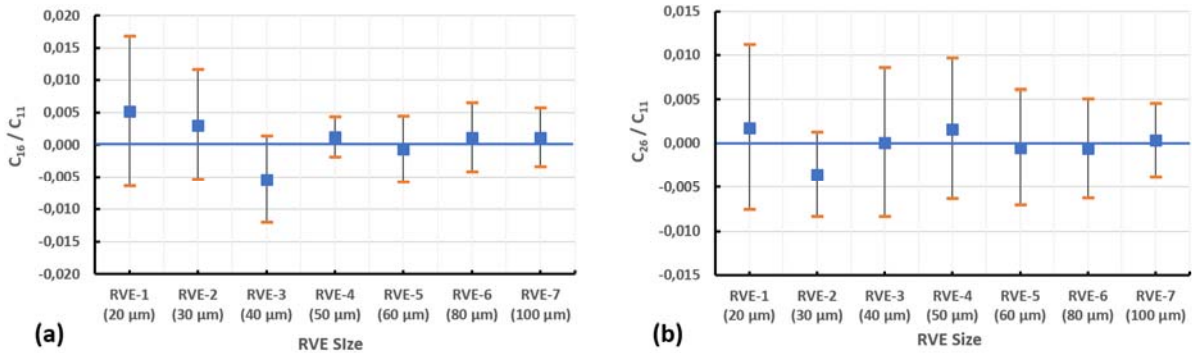


**Fig. 16.** Variation of the ratios  $C_{16}/C_{11}$  (a) and  $C_{26}/C_{11}$  (b) with standard deviations according to the RVE size

The value of the  $C_{22}/C_{11}$  ratio converges to 1 from a size equal to  $50 \mu\text{m}$  with a maximum variation of 2%. The same trend is observed for the  $C_{16}/C_{11}$  and  $C_{26}/C_{11}$  ratios which converge to zero with a maximum variation of 0,5%. The components  $C_{16}$  and  $C_{26}$  are very weak or even null in comparison to  $C_{11}$  and  $C_{22}$ . To evaluate the isotropy of the composite, the  $2 C_{66}/(C_{11} - C_{12})$  ratio, named the Zener anisotropy index [51], must be equal to 1. This ratio increases with the RVE size and converges to an average value between 0.95 and 0.99 for RVE sizes between  $50 \mu\text{m}$  and  $80 \mu\text{m}$  (Fig. 15-b). However,

for a size equal to  $100 \mu\text{m}$ , the ratio increases quite significantly and becomes greater than 1. The composite can then be considered not perfectly isotropic and shows a slight cubic behaviour. This behaviour was also observed by Gentieux et al. [24] for composite materials made of very soft matrix (3 GPa) and stiff particles (450 GPa) with a volume fraction of 40% and by Catapano et al. [36] for particulate-polymer composites made of epoxy matrix and glass particles. The isotropic and cubic stiffness tensors are characterized by 2 and 3 elastic constants, respectively. A VER with an edge equal to  $50 \mu\text{m}$  seems to be acceptable to represent the microstructure of printed green parts. An isotropic or a weak cubic elastic material, in the following of this study, can be considered. The stiffness matrix can be reduced, in case of plane strains and for an isotropic material, as:

$$C_{ij} = \begin{pmatrix} C_{11} & C_{12} & 0 \\ C_{12} & C_{11} & 0 \\ 0 & 0 & C_{66} \end{pmatrix} = \frac{E}{(1+\nu)(1-2\nu)} \begin{pmatrix} 1-\nu & \nu & 0 \\ \nu & 1-\nu & 0 \\ 0 & 0 & \frac{1-2\nu}{2} \end{pmatrix} \quad (23)$$

From Eq. 23, the homogenized Young's modulus  $E$ , Poisson's ratio  $\nu$  and shear modulus  $G$  for an isotropic material, can be expressed as:

$$E = \frac{(C_{11} + 2 C_{12})(C_{11} - C_{12})}{C_{11} + C_{12}} \quad (24)$$

$$\nu = \frac{C_{12}}{C_{11} + C_{12}} \quad (25)$$

$$G = C_{66} = \frac{E}{2 \cdot (1 + \nu)} \quad (26)$$

For an elastic cubic material, the shear modulus  $G$  is equal to  $C_{66}$  and does not depend upon the Young's modulus and Poisson's ratio.

The variation of  $E$  according to the RVE size is plotted in Fig. 17-a. The average value of  $E$  is equal to 1,65 GPa from a VER size of 50  $\mu m$  with a maximum variation less than 5% for the ten generated microstructures (Fig.17-b).

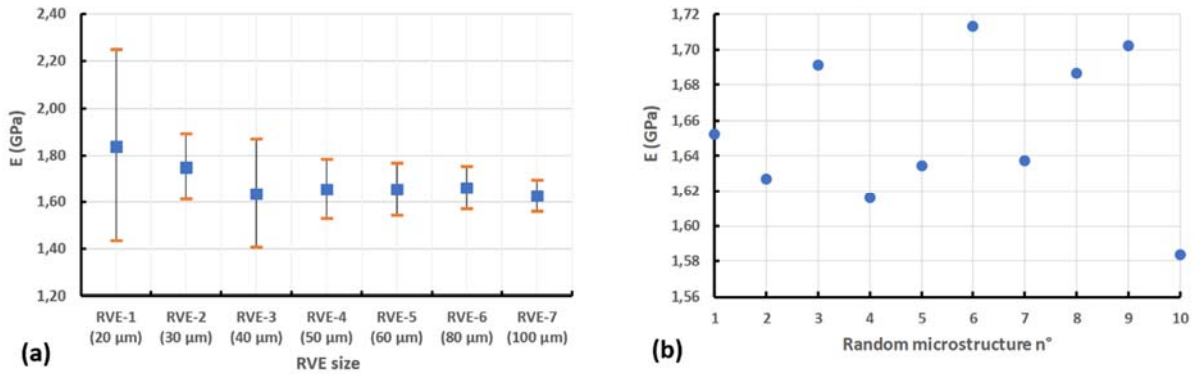


**Fig. 17.** Evolutions of  $E$  according to the RVE size with standard deviations (a) and the random microstructures for a RVE size equal to 50  $\mu m$  (b)

### 3.3.2. Elastic properties prediction from the microscopic model and comparison with analytical homogenization models - experimental results

The developed microscopic model is applied to the design of experiments in order to evaluate the elastic properties of green parts for the various manufacturing parameters tested. Concerning the Young's modulus, the numerical results, obtained for random microstructures and the square and hexagonal arrangements, with a ceramic inclusions volume fraction of 58%, are compared to experimental data and to those from analytical models. The size of square and hexagonal arrangements is identical to the RVE size with a random distribution i.e. 50  $\mu m$ .

The Fig. 18 represents the evolution of the Young's modulus, for the various manufacturing parameters tested, obtained from the analytical homogenization (Reuss and Hashin–Shtrikman lower (HS-) bounds), the homogenization model (random distribution, square and hexagonal arrangements) and experimental data.

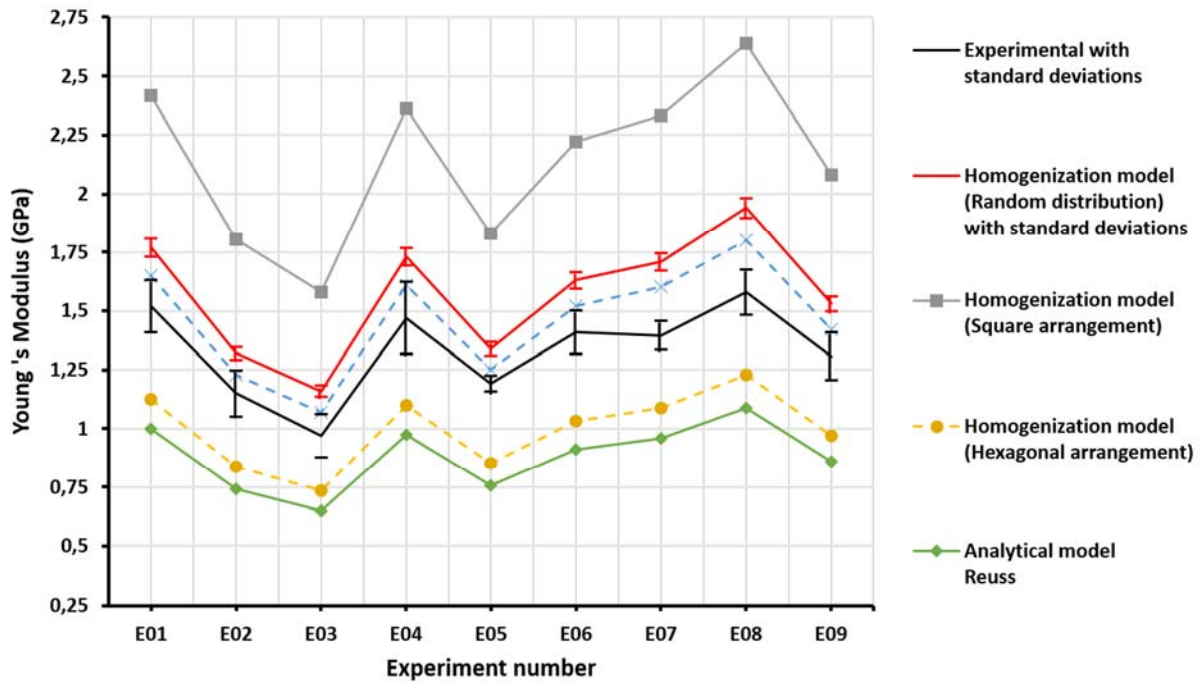


**Fig. 18.** Comparison between experimental, numerical and analytical Young's modulus results according to manufacturing parameters

The analytical models of Voigt and Hashin–Shtrikman higher (HS+) bounds are not studied in this section because the Young's modulus values obtained for printed green parts are very high (about 140 GPa for HS+ limit and about 200 GPa for Reuss limit). These analytical models are not suitable for composite materials with phases with a strong contrast in mechanical properties [24].

The same trend is observed between experimental results and those obtained from analytical and numerical models. The analytical Reuss model and the numerical model with hexagonal arrangement underestimate the value of Young's modulus. In contrary, the analytical HS- model and the numerical model with square arrangement and random distribution of inclusions overestimate the value of Young's modulus. The value of Young's modulus obtained for each model is compared to experimental results with corresponding relative error listed in Table 4. The numerical models with square and hexagonal arrangements which exhibit a cubic symmetric behaviour and the Reuss bound model seem not adapted for the evaluation of the Young's modulus of our polymer/ceramic green parts. The analytical HS- model seems to be the best to predict the Young's modulus with a maximal relative error equal to 17,7 % (E08 experiment). Values obtained from the numerical model with a random distribution are close to those

calculated with HS- bound model. This observation highlights that the ceramic green parts printed by stereolithography can be considered isotropic. The periodic homogenization method, with a random distribution of ceramic particles in the organic matrix, remains an interesting tool to predict the Young's modulus despite significant deviations from experimental measurements and a large relative error with a maximum of 22,8 % (E08 experiment). Infrared spectroscopy measurements ( $400 - 3400 \text{ cm}^{-1}$ ) performed on a green alumina part, a pure polymerized resin part, a photosensitive alumina paste and a photosensitive resin, showed that polymerization does not bring any additional peak to the spectra that could account for the creation of new strong bonds between the cured resin and the surface of the alumina inclusions. Only the weak polymer-alumina interactions, present in the photosensitive alumina paste, remain visible. So perfectly bonded interfaces assumption is not really appropriate to study the overall elastic properties of alumina green parts printed by stereolithography process.

**Table 4**

Comparison between experimental, numerical and analytical Young's modulus results and corresponding relative error between experimental and modelling results according to manufacturing parameters

Experiment	Experimental data	Homogenization models						Analytical models			
		Random distribution		Square arrangement		Hexagonal arrangement		Reuss bound		HS-bound	
		E (GPa)	Relative error (%)	E (GPa)	Relative error (%)	E (GPa)	Relative error (%)	E (GPa)	Relative error (%)	E (GPa)	Relative error (%)
E01	1,52	1,77	16,45	2,42	37,13	1,13	25,92	1,02	32,89	1,70	11,84
E02	1,15	1,32	14,78	1,80	36,22	0,84	27,09	0,76	33,91	1,27	10,43
E03	0,97	1,16	19,59	1,58	38,57	0,73	24,35	0,67	30,93	1,11	14,43
E04	1,47	1,73	17,69	2,36	37,76	1,10	25,18	1,00	31,97	1,66	12,93
E05	1,19	1,34	12,42	1,83	34,90	0,85	28,56	0,77	35,40	1,29	8,22
E06	1,41	1,63	15,60	2,22	36,56	1,03	26,63	0,94	33,33	1,57	11,35
E07	1,40	1,71	22,49	2,33	40,19	1,09	22,15	0,99	29,08	1,64	17,48
E08	1,58	1,94	22,78	2,64	40,17	1,23	22,12	1,12	29,11	1,86	17,72
E09	1,31	1,53	16,97	2,08	37,20	0,97	25,90	0,88	32,72	1,47	12,39

Concerning the Poisson’s ratio (Table 5), we have noticed that it is not dependent of the manufacturing parameters whatever the model. The homogenization model with a random distribution and the analytical HS- bound model predict the same value. The both models (homogenization with a hexagonal arrangement and Reuss bound) seem to overestimate the Poisson’s ratio while the homogenization model with a square arrangement underestimates it.

**Table 5**

Comparison between numerical and analytical Poisson’s ratio results

	Experimental data	Homogenization models			Analytical models	
		Random distribution	Square arrangement	Hexagonal arrangement	Reuss bound	HS-bound
Poisson's ratio	-	0,35	0,26	0,4	0,4	0,35

From the previous analysis of effective Young’s modulus and Poisson’s ratio, the ceramics green parts behave like isotropic materials. To confirm this hypothesis, the shear modulus obtained with the numerical model with a random distribution and the HS- analytical model is compared and listed in Table 6. The values obtained from numerical model, considering an isotropic or cubic elastic symmetry, and analytical model are close and confirm that the ceramic green parts exhibit an isotropic elastic behaviour in the printing plane.

**Table 6**

Comparison between numerical (random distribution) and analytical (HS-) shear modulus results according to manufacturing parameters

Experiment		E01	E02	E03	E04	E05	E06	E07	E08	E09
<hr/>										
$G$ (GPa)										
Analytical model										
HS- bound		0,628	0,468	0,410	0,613	0,475	0,577	0,606	0,686	0,541
	Isotropic symmetry									
$G$ (GPa)	$G = E/(2(1+\nu))$	0,658	0,491	0,430	0,644	0,499	0,605	0,636	0,720	0,568
Numerical model										
Random	Elastic cubic symmetry									
distribution	$G = C_{66}$	0,652	0,487	0,426	0,638	0,494	0,599	0,630	0,713	0,562
<hr/>										

#### 4. Conclusion and perspectives

Predicting the rigidity of green parts, according to manufacturing parameters, is one of key points to optimize the stereolithography process to produce ceramic parts. The objective of this study was to examine the possibility to predict elastic properties and in particular the Young's modulus of green parts manufactured by stereolithography, by developing two numerical models at macroscopic and microscopic scales.

The first developed model consists to establish a relation between the exposure received during the UV insolation and the Young's modulus of the manufactured green parts. The coupling of exposure numerical simulations, which compute the global maximum exposure with the experimental determination of the Young's modulus, has enabled the determination of the variation of the rigidity by identification of a stiffness factor, specific to the ceramic curable system. This model is able to provide Young's modulus with a good level of accuracy and may be extended to 3D to reach a better prediction. A second approach, at a microscopic scale, was to consider the ceramic green part like a polymer/ceramic composite and to evaluate the elastic properties by applying the periodic homogenization technique to a 2D finite element model. After determining the minimum size of the RVE, three arrangements (random distribution, square and hexagonal) have been analyzed in the printing plane. The numerical model with a random distribution of inclusions leads to a good prediction of the Young's modulus despite an overestimation (relative error < 23%). An analyze of effective

elastic properties highlights that a green part containing 58 vol. % alumina particles, with a random distribution, behaves as an equivalent homogeneous material that shows an isotropic response. So, the two independent elastic properties (Young's modulus and Poisson's ratio) are sufficient to characterize the ceramic green parts, in the case of linear elastic behaviour.

Although the HS- analytical model gives better elastic properties than the numerical model with a random distribution, the latter has several advantages for predicting the overall elastic properties of green ceramic parts printed by stereolithography process and remains a promising numerical tool. This 2D model can be improved to take account an imperfect interface between each inclusion and the matrix as a thin interphase consisting of a single homogeneous layer, with properties that are different from the properties of ceramic inclusions and polymer matrix. In this case, the green part will be considered like a three-phase composite. A numerical optimization stage will be necessary to determine the thickness and the rigidity of the thin interphase in order to correlate the experimental and numerical results. The 2D digital model can be extended to 3D which will permit, first of all, to represent the real shape of the inclusions and not to consider the hypothesis of a plane deformation. Moreover, since the lower layers receive more energy than the upper layers during construction, the conversion rate is not uniform across the thickness of the parts. This leads to a stiffness gradient depending on the thickness of the part. In this latter context and at a mesoscopic scale, the 3D RVE can be built with several layers as a laminated composite, each with its own mechanical properties in order to predict the overall elastic properties and analyze the anisotropy of the printed parts.

## References

- [1] T. Chartier, C. Chaput, F. Doreau, M. Loiseau, Stereolithography of structural complex ceramic parts, *J. Mater. Sci.*, 37, (2002), 3141-3147.
- [2] M. L. Griffith and J. W. Halloran, "Freeform Fabrication of Ceramics via Stereolithography," *J. Am. Ceram. Soc.*, 79, (10), (1996), 2601–2068.

- [3] D. T. Pham and R. S. Gault, A comparison of rapid prototyping technologies, *Int. J. Mach. Tools Manuf.*, 38, (10), (1998), 1257-1287.
- [4] T. Chartier and A. Badev, Chapter 6.5 - Rapid Prototyping of Ceramics, in *Handbook of Advanced Ceramics (Second Edition)*, S. Somiya, Éd. Oxford: Academic Press, (2013), p. 489-524.
- [5] J. Brie, T. Chartier, C. Chaput, C. Delage, B. Pradeau, F. Caire, M.P. Boncoeur and J.J. Moreau, A new custom made bioceramic implant for the repair of large and complex craniofacial bone defects, *J. Cranio-Maxillo-Fac. Surg.*, 41, (2013), 403-407.
- [6] T. Chartier, C. Dupas, M. Lasgorceix, J. Brie, N. Delhote, and C. Chaput, Additive Manufacturing to Produce Complex 3D Ceramic Parts, *J. Ceram. Sci. Technol.*, 6, (2), (2014), 95-104.
- [7] A. Zocca, P. Colombo, C. M. Gomes, and J. Günster, Additive Manufacturing of Ceramics: Issues, Potentialities, and Opportunities, *J. Am. Ceram. Soc.*, 98, (7), (2015), 1983-2001.
- [8] J. Raynaud, V. Pateloup, M. Bernard, D. Gourdonnaud, D. Passerieux, D. Cros, V. Madrangeas and T. Chartier, Hybridization of additive manufacturing processes to build ceramic/metal parts: Example of LTCC, *J. Eur. Ceram. Soc.*, 40, (2020), 759-767.
- [9] D. Wu, Z. Zhao, Q. Zhang, H. J. Qi and D. Fang, Mechanics of shape distortion of DLP 3D printed structures during UV post-curing, *R. Soc. Chem., Soft Matter*, 15, (2019), 6151-6159
- [10] P.F. Jacobs, *Rapid Prototyping & Manufacturing: Fundamentals of Stereolithography - Chapter 4 - Fundamental Processes*, Soc. Manuf. Eng., 1992.
- [11] Y. Huang, M. C. Leu, J. Mazumder and A. Donmez, Additive Manufacturing: Current State, Future Potential, Gaps and Needs, and Recommendations, *ASME J. Manuf. Sci. Eng.*, 137, (2015).

- [12] J. Tarabeux, V. Pateloup, P. Michaud and T. Chartier, Development of a numerical simulation model for predicting the curing of ceramic systems in the stereolithography process, *J. Eur. Ceram. Soc.*, 38, (2018), 4098-4098.
- [13] S. Westbeek, J.A.W. Van Dommelen, J.J.C. Remmers and M.G.D. Geers, Multiphysical modeling of the photopolymerization process for additive manufacturing of ceramics, *Eur. J. Mech., A Solids*, 71, (2018), 210–223.
- [14] F. Azarmi and I. Sevostianov, Evolution of thermo-mechanical properties in the process of alumina manufacturing using laser stereolithography technique, *Int. J. Eng. Sci.*, 144, (2019), 1-11.
- [15] Y. Yang, L. Li and J. Zhao, Mechanical property modeling of photosensitive liquid resin in stereolithography additive manufacturing: Bridging degree of cure with tensile strength and hardness, *Mat. Des.*, 162, (2019), 418–428.
- [16] T. Chartier, C. Dupas, P. M. Geffroy, V. Pateloup, M. Colas, J. Cornette and S. Guillemet-Fritschb, Influence of irradiation parameters on the polymerization of ceramic reactive suspensions for stereolithography, *J. Eur. Ceram. Soc.*, 37, (2017), 4431-4436.
- [17] 3D Ceram (Limoges, France- <http://3dceram.com>)
- [18] B. Pan, K. Qian, H. Xie and A.Asundi, Two-dimensional digital image correlation for in-plane displacement and strain measurement: a review, *Measurement Sci. and Technol.* , 20, (6), (2009), 17p.
- [19] M. Babaeian and M. Mohammadimehr, Investigation of the time elapsed effect on residual stress measurement in a composite plate by DIC method, *Optics and Lasers in Engineering*, 128, (2020), 11p.

- [20] P.M.C. Carneiro, P.V. Gamboa, C. Baudín and A. P. Silva, Modelling of elastic modulus of a biphasic ceramic microstructure using 3D representative volume elements, *J. Eur. Ceram. Soc.*, 40, (2020), 901-910.
- [21] Z. Hashin and S. Shtrikman, On some variational principles in anisotropic and nonhomogeneous elasticity, *J. Mech. Phys. Solids*, 10, (4), (1962), 335-342.
- [22] Z. Hashin and S. Shtrikman, A variational approach to the theory of the elastic behaviour of multiphase materials, *J. Mech. Phys. Solids*, 11, (2), (1963), 127-140.
- [23] Z. Hashin, On elastic behaviour of fibre reinforced materials of arbitrary transverse phase geometry, *J. Mech. Phys. Solids*, 13, (3), (1965), 119-134.
- [24] T. Gentieu, A. Catapano, J. Jumel and J. Broughton, Computational modelling of particulate-reinforced materials up to high volume fractions: Linear elastic homogenisation, *Proc IMechE, Part L: J. Mat: Design and Applications* (2016), 16p.
- [25] K. Sab, On the homogenization and the simulation of random materials. *Eur. J. Mech. Solids* 11, (1992), 585–607.
- [26] W. J. Drugan and J. R. Willis, A micromechanics-based nonlocal constitutive equation and estimates of representative volume element size for elastic composites, *J. Mech. Phys. Solids*, 44, (1996), 497-524.
- [27] M. Ostoja-Starzewski, Random field models of heterogeneous materials. *Int. J. Solids Struct.*, (35), (1998), 2429–2455.
- [28] P. Evesque, Fluctuations, correlations and representative elementary volume (REV) in granular materials, *Poudres & Grains*, 11, (2000), 6-17.

- [29] T. Kanit, S. Forest, I. Galliet, V. Mounoury and D. Jeulin, Determination of the size of the representative volume element for random composites: statistical and numerical approach, *Int. J. Solids Struct*, 40, (2003), 3647-3679.
- [30] M. Gitman and H. Askes, Quantification of stochastically stable representative volumes for random heterogeneous materials, *Arch. Appl. Mech.*, 75, (2006), 79–92.
- [31] I. M. Gitman, H. Askes H. and L. I. Sluys, Representative volume: Existence and size determination, *Engineering Fracture Mechanics*, 74, (2007), 2518–2534.
- [32] C. Pelissou, J. Baccou, Y. Monerie and F. Perales, Determination of the size of the representative volume element for random quasi-brittle composites, *Int. J. Solids Struct*, 46, (2009), 2842–2855.
- [33] S. Kari, H. Berger, R. Rodriguez-Ramos and U. Gabbert, Computational evaluation of effective material properties of composites reinforced by randomly distributed spherical particles, *Compos. Struct.*, 77, (2007), 223-231.
- [34] S. Fu, X. Feng X, B. Lauke and Y. W. Mai, Effects of particle size, particle/matrix interface adhesion and particle loading on mechanical properties of particulate–polymer composites, *Compos. part B*, 39, (2008), 933–961.
- [35] S. Nemat-Nasser and M. Hori, *Micromechanics: overall properties of heterogeneous materials*. 37, (2013), North Holland: Elsevier.
- [36] A. Catapano and J. Jumel, A numerical approach for determining the effective elastic symmetries of particulate-polymer composites, *Compos. Part B*, 78, (2015), 227-243.

- [37] W. Han, A. Eckschlager and H. J. Böhm, The effects of three-dimensional multi-particle arrangements on the mechanical behavior and damage initiation of particle reinforced MMCs, *Compos. Sci. Technol*, 61, (2001), 1581–1590.
- [38] J. Segurado, C. Gonzalez and J. LLorca, A numerical investigation of the effect of particle clustering on the mechanical properties of composites, *Acta Materialia*, 51, (2003), 2355–2369.
- [39] K. Terada, M. Hori, T. Kyoya and N. Kikuchi, Simulation of the multi-scale convergence in computational homogenization approaches, *Int. J. Solids Struct*, 37, (2000), 228-2311.
- [40] F. Larsson, K. Runesson, S. Saroukhani and R. Vafadari, Computational homogenization based on a weak format of micro-periodicity for RVE-problems, *Comput. Methods Appl. Mech. Engrg.*, 200, (2011), 11–26.
- [41] V.D. Nguyen, E. Bechet, C. Geuzaine, and L. Noels, Imposing periodic boundary condition on arbitrary meshes by polynomial interpolation, *Comput. Mater. Sci.*, 55, (2012), 390–406.
- [42] <https://www.salome-platform.org>
- [43] D. Ali and S. Sen, Finite element analysis of the effect of boron nitride nanotubes in beta tricalcium phosphate and hydroxyapatite elastic modulus using the RVE model, *Compos. Part B*, 90, (2016), 336-340.
- [44] L. Riaño and Y. Joliff, An ABAQUS™ plug-in for the geometry generation of representative Volume Elements with randomly distributed fibers and interphases, *Compos. Struct.*, 209, (2019), 644–651.

- [45] V. Mityushev and W. Nawalaniec, Effective conductivity of a random suspension of highly conducting spherical particles, *Appl. Math. Modelling*, 72, (2019), 230–246.
- [46] Y. Pan, L. Iorga and A. A. Pelegri, Analysis of 3D random chopped fiber reinforced composites using FEM and random sequential adsorption, *Comput. Mater. Sci.*, 43, (2008), 450–461.
- [47] J.C. Michel, H. Moulinec and P. Suquet, Effective properties of composite materials with periodic microstructure: a computational approach, *Comput. Methods Appl. Mech. Engrg.*, 172, (1999), 109–143.
- [48] R. Hill, The essential structure of constitutive laws for metal composites and polycrystals, *J. Mech. Phys. Sol.*, 15, (1967), 79-95.
- [49] P. J. Bartolo, *Stereolithography: Materials, Processes and Applications*. Springer Science & Business Media.
- [50] R. Deterre and G. Froyer, *Introduction aux matériaux polymères (2<sup>ème</sup> Ed.)*. Tec et doc- Lavoisier, (2016).
- [51] R. Grasset-Bourdel, A. Alzina, N. Tessier-Doyen, N. Schmitt, M. Huger, T. Chotard, D. Gruber and H. Harmuth, Optimisation of 3D RVE for anisotropy index reduction in modelling thermoelastic properties of two-phase composites using a periodic homogenisation method, *Comput. Mater. Sci.*, 50, (2011), 3136–3144.